

# Resonant Light Guiding Along a Chain of Silicon Nanoparticles

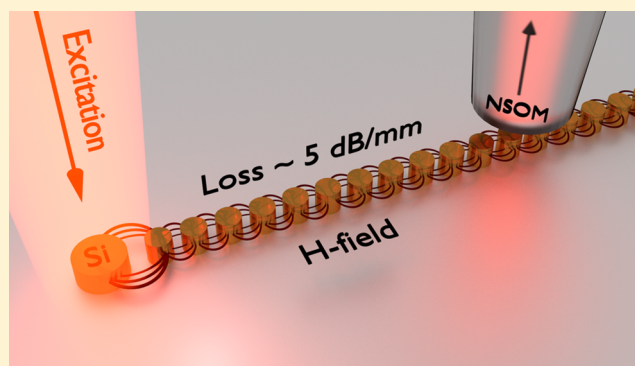
Reuben M. Bakker,<sup>\*,†</sup> Ye Feng Yu,<sup>†</sup> Ramón Paniagua-Domínguez,<sup>†</sup> Boris Luk'yanchuk, and Arseniy I. Kuznetsov

Data Storage Institute, A\*STAR (Agency for Science, Technology and Research), 2 Fusionopolis Way, 138634, Singapore

## Supporting Information

**ABSTRACT:** Subwavelength confined waveguiding is experimentally demonstrated with high refractive index dielectric nanoparticles with photon energy propagation at distances beyond 500  $\mu\text{m}$ . These particles have naturally occurring electric and magnetic dipole resonances. When they are placed in a 1D chain, the magnetic resonances of adjacent elements couple to each other, providing a means to transport energy at visible or NIR wavelengths in a confined mode. Chains of nanoparticles made of silicon were fabricated and guided waves were measured with near-field scanning optical microscopy. Propagation loss is quantified at 34 dB/mm for 720 nm and 5.5 dB/mm for 960 nm wavelengths with 150 and 220 nm diameter particles, respectively. Simulations confirm the unique properties of this waveguiding in comparison with photonic crystals. The resonant nature of the waveguide lays a foundation for integrated photonics beyond nanowire waveguides of silicon and silicon nitride. This technology is promising for more compact and deeper photonic integration such as right angle bends, more compact modulators, slow light and interfacing with single photon emitters for photonic integrated circuits, quantum communications, and biosensing.

**KEYWORDS:** Silicon nanoparticle, silicon photonics, waveguide, optically induced magnetic resonances, NSOM



Guiding photon energy on the nanometer scale is a continuous goal of the photonics community with broad applications in the physical and biomedical sciences.<sup>1–6</sup> This provides opportunity to shrink interconnect technology and ultimately increase communication bandwidth for inter- and intrachip applications. Modern plasmonics holds promise for this task through schemes such as surface plasmon polaritons,<sup>1</sup> coupling of localized surface plasmon resonances along a chain of nanoparticles<sup>2,3</sup> and combining plasmonic and dielectrics for guiding energy.<sup>4–6</sup> Though plasmonics offers superior energy localization on the subwavelength scale, waveguiding suffers from losses induced by the metal.

An alternative to plasmonics for manipulating light at the subwavelength scale is high-index dielectric nanoparticle based nanophotonics.<sup>7–22</sup> For example, silicon with a refractive index of  $\sim 4$  offers the opportunity to tune both an electric dipole and magnetic dipole response at visible and NIR wavelengths.<sup>7–12</sup> Compared to plasmonics, this system has significantly lower material losses and there are two fundamental dipole resonances (electric and magnetic) to use in system engineering. Resonances from one particle can couple to an adjacent particle in a near lossless manner through dipole–dipole interaction<sup>13–16</sup> and for multiple nanoparticles, waveguiding occurs. These systems are different from 1D photonic crystals<sup>23</sup> and subwavelength grating waveguides<sup>24</sup> because the individual elements are resonant at the wavelength of interest. This effect has been explored theoretically,<sup>18–21</sup> through simulations<sup>20–22</sup> and demonstrated experimentally in the gigahertz spectral

range.<sup>20,21</sup> However, no experimental evidence at optical frequencies has been reported.

When fully developed, high-index dielectric nanoparticle-based nanophotonics will be complementary to traditional integrated photonics with nanowire waveguides such as those made of silicon for near-infrared (NIR) light<sup>25–28</sup> and silicon nitride for visible (VIS) light.<sup>29</sup> Significant efforts over the past 20+ years have brought this technology forward with a vast component library and device development toward commercialization. This stated goal of DARPA is nicely summarized in ref 30. As integrated photonics continues to mature, it is pertinent to develop complementary technology for deeper system integration, miniaturization, and potentially higher bandwidth interconnects.

This work is the first experimental demonstration of subwavelength waveguiding through resonant dielectric nanoparticle chains at visible, 720 nm, (cylindrical nanoparticles with a diameter,  $D$ , and height,  $H$ , of 150 nm) and NIR, 960 nm, ( $D$  and  $H$  of 220 nm) wavelengths along a chain of resonant silicon nanoparticles. Loss is measured at  $34 \pm 1.3$  dB/mm for 720 nm and  $5.5 \pm 0.7$  dB/mm for 960 nm wavelengths. Dimensions have been chosen so that the single nanoparticle resonates at the wavelength of interest. Full field numerical simulations

**Received:** January 26, 2017

**Revised:** April 24, 2017

**Published:** May 2, 2017

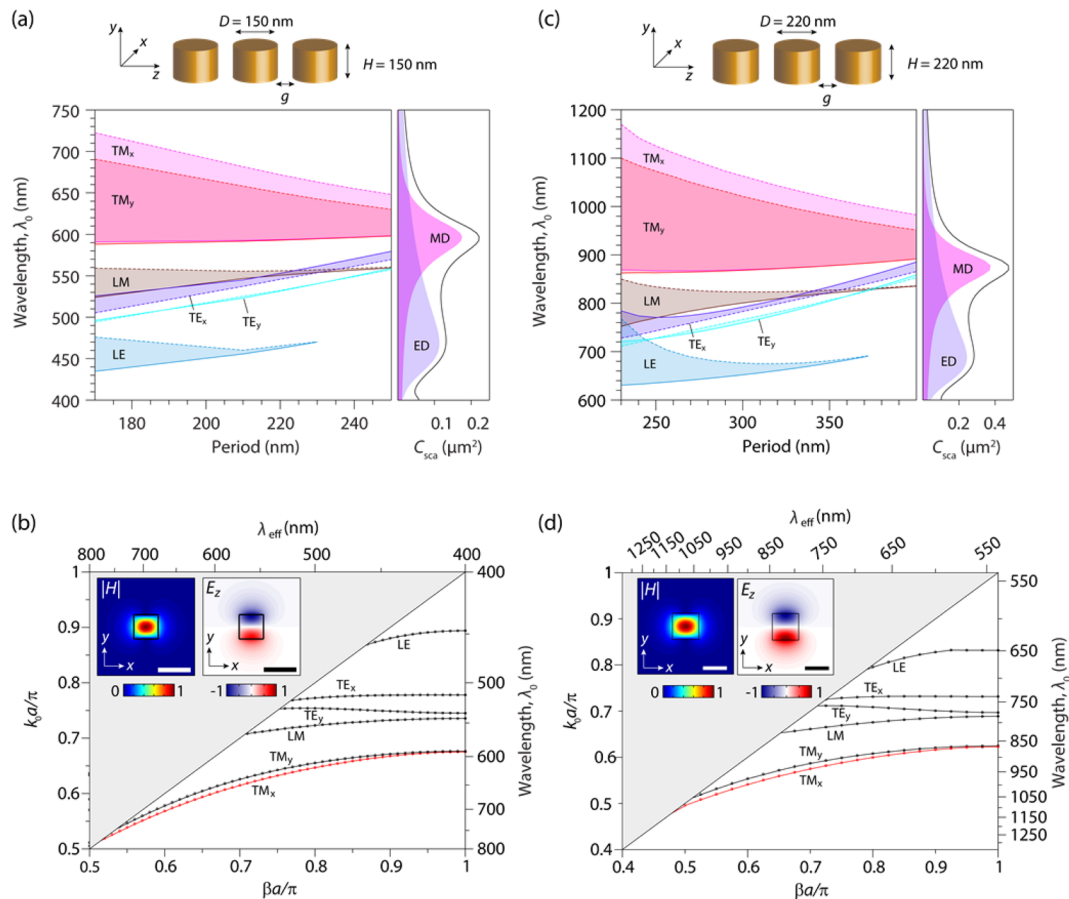


**Figure 1.** Basic modes of the silicon nanoparticle waveguide for 150 nm (a,b) and 220 nm (c,d) dimensioned nanoparticles from numerical calculations with lossless material parameters. (a,c) The left panels show the modes as a function of period (gap between the particles) and the right panels the scattering spectra and dipolar contributions from a single particle ( $D$ , diameter;  $g$ , gap;  $H$ , height;  $\lambda_0$ , free space wavelength,  $k_0 = 2\pi/\lambda_0$ ; TM, transverse magnetic; LM, longitudinal magnetic; TE, transverse electric; LE, longitudinal electric;  $C_{\text{sca}}$ , scattering cross section; ED, electric dipole; MD, magnetic dipole). (b,d) Dispersion plots for a 50 nm gap (see SI Figure S1 for dispersion plots including material loss); insets illustrate the magnetic and electric field distributions through the middle of a single nanoparticle for the fundamental,  $\text{TM}_x$  mode ( $\lambda_{\text{eff}}$ , effective wavelength;  $\beta$ , propagation constant,  $a$ , period). Scale bars represent 200 nm (see SI Figure S2 for profiles of the other modes).

(Comsol Multiphysics and Lumerical FDTD) are used to complement and expand the understanding of the experimental results.

A design study is presented in Figure 1 to provide insights into the waveguiding properties of the nanoparticle chain for visible and NIR with lossless material parameters. Transmission bands, the shaded areas, as a function of the nanoparticle period (Figure 1a,c) and the dispersion relation for a gap between neighboring nanoparticles of  $g = 50$  nm (Figure 1b,d) are provided. The 50 nm gap is chosen for its combination of strong coupling between particles, wide bandwidth of the primary mode, and fabrication feasibility. Although the fundamental mode has no strict cutoff, a lower-energy limit for waveguiding is considered when the mode approaches the light line and confinement becomes negligible.

Mode analysis is performed by full numerical simulations using the finite elements method (Comsol Multiphysics). A single unit cell of the chain is simulated and Bloch boundary conditions are applied in the propagation direction with the Bloch vector magnitude given by the propagation constant  $\beta \in (0, \pi/a)$ , with  $a$  being the period of the array. The dispersion relation is retrieved by calculating the eigenmodes and associated eigenfrequencies of the system for each value of  $\beta$ . Silicon material parameters are taken from ellipsometric

measurements of the deposited films; losses are neglected in this calculation.

The dominant transmission mode of the chain is the transverse magnetic (TM-like) mode, characterized by a distribution of electric and magnetic fields within the particles that resembles a magnetic dipole. This mode is different than what is reported for photonic crystal (PC) modes in chains of nanoparticles where the main mode is TE.<sup>31,32</sup> For the presented geometry, there are two similar TM modes, one for vertically oriented (parallel to the cylinder axis) and one for horizontally oriented (perpendicular to both the cylinder axis and the propagation direction) dipole modes of the particles (as shown in Supporting Information (SI) Figure S2). The mode for the horizontal dipoles, highlighted in red in the dispersion relation, is the one experimentally demonstrated in this work.

The spectral position of the band gap edge shows a weak dependence on the periodicity of the array and is mainly determined by the magnetic dipole resonance of the individual silicon nanoparticles. This can be seen in the right-hand panels of Figure 1a,c, which show the total scattering efficiency, together with the electric and magnetic dipole contributions from a single cylinder (illuminated by a plane wave propagating along its axis). These modes are contrary to the modes of PC

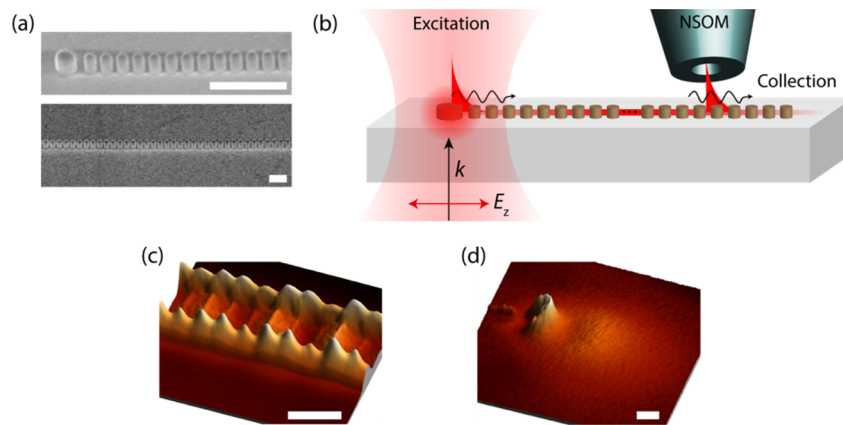


**Figure 2.** Experimental measurement of waveguiding through chains of silicon nanoparticles. (a) Scanning electron microscope image of the Silicon Nanoparticle Waveguide for 150 nm case. (b) Measurement setup showing the excitation of the waveguide with linearly polarized light focused on the origin and collection of evanescent fields with an uncoated NSOM tip from different sections of the waveguide. (c) A representative near-field microscopy image of the waveguide mode. This image is taken with a wavelength of 720 nm, 400  $\mu\text{m}$  away from the origin. (d) A representative near-field microscopy image of the end point of the waveguide. This image is taken with a wavelength of 720 nm, 580  $\mu\text{m}$  away from the origin. All scale bars are 500 nm.

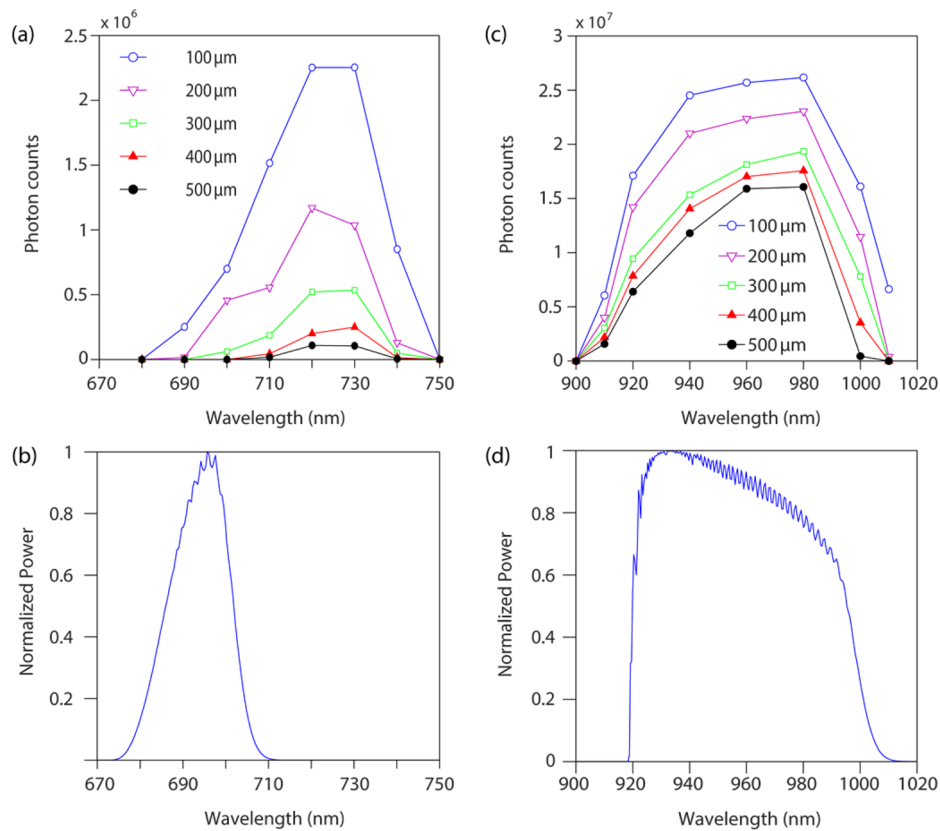


**Figure 3.** Near-field scanning optical microscopy transmission measurements as a function of wavelength for visible (a) and NIR (c) waveguides compared with simulations for visible (b) and NIR (d). (a,c) Photon counts taken over multiple unit cells of nanoparticles, plotted as a function of excitation wavelength for distances of 100, 200, 300, 400, and 500  $\mu\text{m}$  away from the waveguide origin. (b,d) Simulated transmission spectrum for the corresponding geometry (see also SI Figure S4).

waveguides where the spectral position of the first band gap is strongly dependent on periodicity.<sup>31,32</sup> This distinct behavior, similar to that of metamaterials when compared to PCs,<sup>31</sup> can be investigated by increasing the periodicity of the chain. For a PC mode, the band edge moves almost linearly with the period; however, in the presented work the TM mode's band edge is virtually unaffected with increasing the period, as seen in Figure 1a,c. Only the total width of the band is affected due to the

reduction of the first Brillouin zone (FBZ) (or the filling fraction from an effective medium perspective). However, the rest of the modes experience a strong shift when the period is modified. Further evidence on distinction from a PC mode is provided by the fact that the TM band is strongly affected when the height of the particles is modified (thus shifting the resonance frequency of the individual particles), as shown in SI Figure S3. We also mention that the primary TM mode exhibits

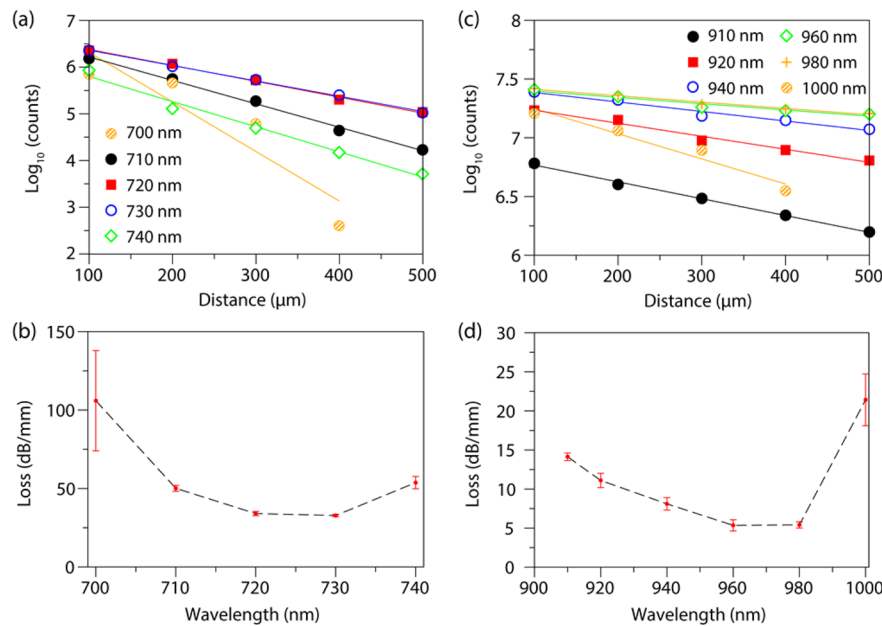


**Figure 4.** Experimental measurements illustrating propagation loss for visible (a,b) and NIR (c,d) waveguides. The experimental results from Figure 3 are plotted to determine loss as a function of wavelength. (a,c) Photon counts are plotted in semilog format as a function of distance from the origin for the different propagating wavelengths. (b,d) Experimental loss as a function of wavelength for the visible and NIR nanoparticle waveguides. Light at 720 nm shows a propagation loss of  $34 \pm 1.3$  dB/mm. Light at 960 nm shows a propagation loss of  $5.5 \pm 0.8$  dB/mm. The error bars originate from the linear regression of the data.

slow light characteristics at the edge of the FBZ, which follows from its vanishing slope in the dispersion relation  $k = k(\omega)$  (recall that in the absence of strong losses  $v_g = \partial\omega/\partial k$ ).

For experimental demonstration, 1D chains of silicon nanocylinders (up to  $580 \mu\text{m}$  long) were fabricated on a quartz substrate. Figure 2a shows characteristic SEM images of the 150 nm particle size waveguide. Fabrication starts with growing amorphous silicon films with thicknesses of 150 and 220 nm on quartz substrates using the inductively coupled plasma chemical vapor deposition technique (Plasmalab System 380, Oxford Instruments). The films are characterized using ellipsometry to extract their material parameters for modeling. Nanopatterning is performed via electron beam lithography (Elionix, 100 kV) with hydrogen silsesquioxane (HSQ, Dow Corning, XR-1541-002) as the resist. The sample is developed using Tetramethylammonium hydroxide (TMAH, 25%). Etching, using the exposed HSQ as a mask, is performed with an inductively coupled plasma etcher (Plasmalab System 100, Oxford). The end result is chains of Si nanoparticles on a quartz substrate. Different chains are fabricated at a  $5 \mu\text{m}$  pitch to avoid crosstalk.

Transmission of light through the waveguides was experimentally confirmed using near-field scanning optical microscopy (NSOM) (Multiprobe SPM/NSOM, Nanonics Imaging). Figure 2b illustrates the measurement procedure. The waveguide is excited at its origin through a  $50\times$  objective lens (0.42NA, Mitutoyo) with linearly polarized light (along the waveguide direction). The light source is a photonic crystal fiber based supercontinuum (SuperK Power, NKT Photonics). Wavelength bands are selected using a variable bandpass filter for the visible portion of the spectrum and an acousto-optical tunable filter for the NIR measurement. An uncoated, aperture type NSOM tip is used to probe the near-fields of the waveguide at selected distances from the waveguide origin. At each distance, multiple scans are performed for different

excitation wavelengths over multiple adjacent unit cells. Photons are counted using an avalanche photodiode and normalized for wavelength efficiency. The background signal, measured away from the waveguide, is subtracted to provide consistent results at different distances from the waveguide origin. NSOM scans are performed at  $100 \mu\text{m}$  intervals along the waveguide.

A typical NSOM image is illustrated in Figure 2c ( $\lambda = 720$  nm,  $400 \mu\text{m}$  away from the origin is illustrated). The majority of the measured field is along the outside edges of the waveguide. A scan at the end point of the line,  $580 \mu\text{m}$  away from the origin, is provided in Figure 2d to show that lightwave energy traverses the entire line. Because of an impedance mismatch at the waveguide's end point, there is an abrupt spike.

Waveguide measurements are compiled as a function of wavelength and distance in Figures 3 and 4. The 150 nm nanoparticle waveguide has peak propagation at a wavelength of 720 nm with losses of  $34 \pm 1.3$  dB/mm and a bandwidth of 30 nm. The 220 nm nanoparticle waveguide has peak propagation at a wavelength of 960 nm with losses of  $5.5 \pm 0.8$  dB/mm and a bandwidth of 90 nm. The reduced loss is expected as amorphous silicon has less material loss at 960 nm compared to 720 nm. Moving further into the NIR (such as 1310 and 1550 nm), we expect an optimally designed system to demonstrate even less loss.

The experimental propagation is directly compared with full numerical FDTD simulations in Figure 3. For the visible-range case, the simulation consists of 200 nanoparticles (height and diameters of 150 nm with a 200 nm period). The data shown is collected from a power monitor  $30 \mu\text{m}$  from the origin. For the NIR case, the simulation consists of 300 nanoparticles (height and diameters of 220 nm with a 270 nm period). The data shown is collected from a power monitor  $70.2 \mu\text{m}$  from the origin. In both cases the system is excited by a localized dipolar source located in the first particle of the chain with appropriate

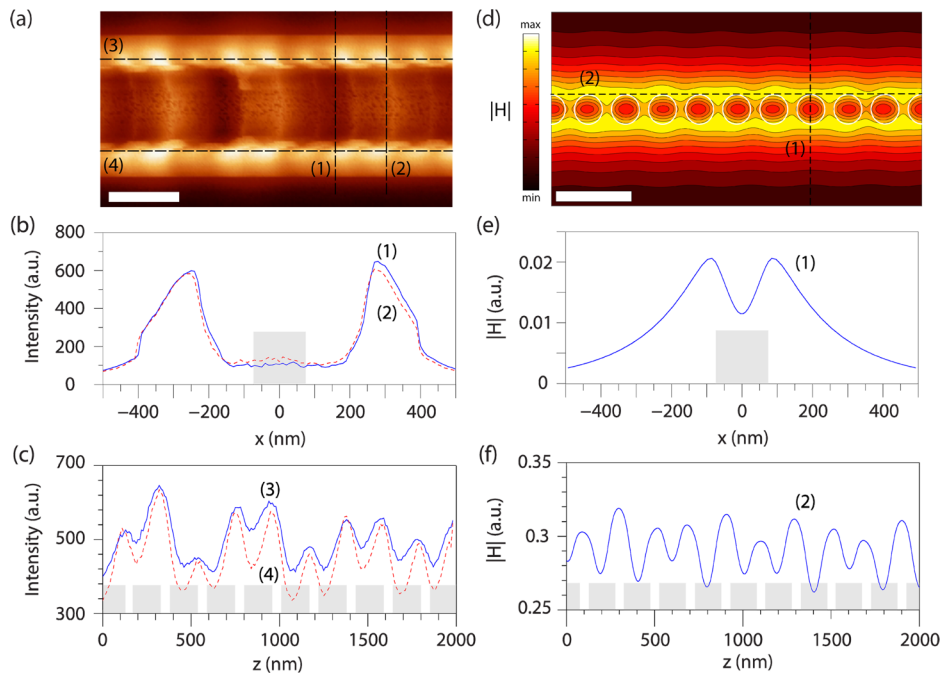


**Figure 5.** Waveguide field profiles for the 150 nm silicon nanoparticle chain at 720 nm wavelength. (a–c) Experimental NSOM data illustrating an *XY* mapping of 10 unit cells a distance of 400  $\mu\text{m}$  away from the line origin showing an NSOM signal intensity map (a) along with cross sections orthogonal (b) and parallel (c) to the chain as marked on the map. (d–f) Numerical simulation data of 10 unit cells showing H field modulus map (d) along with cross sections orthogonal (e) and parallel (f) to the chain as marked on the field map. The fields are taken 20 nm above the structures. The scale bars in (a,d) are 400 nm and the position of the particles indicated in gray in (b,c) and (d,e).

dipole moment. The presence of the substrate is considered and the whole simulation domain is surrounded by perfectly matched layers to absorb any out-going radiation. The minor ringing effects in the simulation curves are due to reflections at the ends of the chain. The simulations compare well with the experimental data except for a wavelength shift for the visible case. This shift is likely due to a difference in the material parameters of the fabricated sample from the deposited films used in the ellipsometry measurements

The dominant, resonant mode of the visible wavelength chain (taken at 720 nm) is illustrated in Figure 5 via experimental (Figure 5a–c) and numerical (Figure 5d–f) field maps with associated cross section plots. The experimental and numerical data show the same features. Though it needs to be mentioned that due to a scanning probe artifact, the experiment shows elongated features orthogonal to the chain when compared to the simulations and actual geometry. Low-field regions are observed at the center of the individual nanoparticles with high-field regions at the nanoparticle edges.

Full-field simulations are performed to view the mode profiles and calculate the transmission spectra, losses, and effective mode area of the nanoparticle waveguide. The 150 nm nanoparticle waveguide has simulated losses of 20 dB/mm with an effective mode area of 0.27  $\mu\text{m}^2$ . The 220 nm nanoparticle waveguide has simulated losses of 2.8 dB/mm with an effective mode 0.24  $\mu\text{m}^2$ . For a full dependence of the loss and effective mode area as a function of wavelength, see SI Figures S4 and S5. For the loss calculation, a set of equally distanced monitors perpendicular to the propagation direction are used to record the net flux of energy as a function of distance. The data from each monitor is normalized to the flux across the first monitor and plotted as a function of distance to retrieve the characteristic loss of the system. In the case of the 150 nm nanoparticles, 20 monitors were considered. In the case of the

220 nm particles, 28 monitors were used. For the computation of the effective mode area the following definition is used

$$A_{\text{eff}} = \frac{(\int S_z dA)^2}{\int S_z^2 dA}$$

where  $S_z$  represents the  $z$ -component of the time-averaged Poynting vector (i.e., in the direction of propagation of the mode).

In comparison with waveguiding of VIS and NIR light in SiN nanowire waveguides,<sup>29</sup> for far-red wavelengths (780 nm) range, unclad SiN nanowire waveguides with a cross-section geometry of 220  $\times$  450 nm demonstrate a loss of 0.4 dB/mm that is an order of magnitude lower than that obtained in our work but the lateral cross-section of the waveguide is >2 times larger. At telecommunication wavelengths, Si waveguides of various material phases have similar losses (crystalline-Si has losses at 0.24 dB/mm with a 220  $\times$  500 nm cross section,<sup>25</sup> poly-Si has losses at 0.62 dB/mm with a 120  $\times$  350 nm cross section,<sup>27</sup> and amorphous-Si has losses at 0.27 dB/mm with a 220  $\times$  500 nm cross section<sup>28</sup>).

The Si nanoparticle waveguides presented in this work provide a footprint that is smaller than traditional SiN and Si waveguides. Currently, this comes at the cost of higher losses though the loss is not prohibitive for transferring photon energy distances well over 100  $\mu\text{m}$ , a reasonable length for intrachip applications. Loss for this system can be improved by adding an upper cladding layer, material engineering and shifting the operating wavelength further to the NIR. Additionally, the resonant nature of the nanoparticle waveguide system holds promise for adding right angle junctions<sup>28</sup> and the compact device functionality this enables. High-field enhancement at the resonance wavelength and slow-light behavior can be taken advantage of for on-chip sensing and laser devices.

In conclusion, this work demonstrates subwavelength confined waveguiding at distances over 500  $\mu\text{m}$  with visible and NIR light. This most fundamental property can be expanded to create a new class of devices, offering control of light on the subwavelength scale without the high losses associated with metal-based nanophotonics and more compact than traditional integrated waveguides. The waveguiding can be scaled both up and down in wavelength with the size of the nanoparticle and choosing a material with the appropriate dielectric function. This work complements existing photonic integration systems and in the future will expand existing schemes for photonic integration with microelectronics, data communications along with on chip fluorescence, and quantum photonic applications.

## ■ ASSOCIATED CONTENT

### Supporting Information

The Supporting Information is available free of charge on the ACS Publications website at DOI: 10.1021/acs.nanolett.7b00381.

Five additional figures (PDF)

## ■ AUTHOR INFORMATION

### Corresponding Author

\*E-mail: Reuben\_bakker@dsi.a-star.edu.sg.

### ORCID

Reuben M. Bakker: 0000-0003-0534-8287

### Author Contributions

R.M.B. performed the near-field experiments and analysis and wrote the first draft of the manuscript. Y.F.Y. performed initial simulations and nanofabrication of the waveguides. R.P.D. performed additional simulations and mode analysis for deeper understanding. B.L. initiated the ideas of this work. A.I.K. initiated the ideas and supervised this work. All authors contributed to the manuscript preparation and reviewed the final version of the manuscript.

### Author Contributions

†R.M.B., Y.F.Y., and R.P.D. contributed equally.

### Funding

The authors at DSI were supported by DSI core funds and A\*STAR SERC Pharos program, Grant 152 73 00025 (Singapore).

### Notes

The authors declare no competing financial interest.

## ■ ACKNOWLEDGMENTS

Fabrication, scanning electron microscope imaging, and NSOM works were carried out in facilities provided by SnFPC@DSI (SERC Grant 092 160 0139). The authors acknowledge Toh Yeow Teck and Leonard Gonzaga (Data Storage Institute) for their contributions to developing the Silicon nanofabrication processes, Vytautas Valuckas (Data Storage Institute) for assistance with SEM imaging, and Dr. Andrey Miroshnichenko (Australian National University) and Dr. Yuan Hsing Fu (DSI) for participation in discussions and simulations at the initial stage of this work.

## ■ REFERENCES

(1) Gramotnev, D. K.; Bozhevolnyi, S. I. Plasmonics beyond the diffraction limit. *Nat. Photonics* **2010**, *4*, 83–91.

(2) Quinten, M.; Leitner, A.; Krenn, J. R.; Aussenegg, F. R. Electromagnetic energy transport via linear chains of silver nanoparticles. *Opt. Lett.* **1998**, *23*, 1331–1333.

(3) Maier, S. A.; Kik, P. G.; Atwater, H. A.; Meltzer, S.; Harel, E.; Koel, B. E.; Requicha, A. A. Local detection of electromagnetic energy transport below the diffraction limit in metal nanoparticle plasmon waveguides. *Nat. Mater.* **2003**, *2*, 229–232.

(4) Dionne, J. A.; Sweatlock, L. A.; Atwater, H. A.; Polman, A. Plasmon slot waveguides: Towards chip-scale propagation with subwavelength-scale localization. *Phys. Rev. B: Condens. Matter Mater. Phys.* **2006**, *73*, 035407.

(5) Oulton, R. F.; Sorger, V. J.; Genov, D. A.; Pile, D. F. P.; Zhang, X. A hybrid plasmonic waveguide for subwavelength confinement and long-range propagation. *Nat. Photonics* **2008**, *2*, 496–500.

(6) Volkov, V. S.; Han, Z.; Nielsen, M. G.; Leosson, K.; Keshmiri, H.; Goscinia, J.; Albrechtsen, O.; Bozhevolnyi, S. I. Long-range dielectric-loaded surface plasmon polariton waveguides operating at telecommunication wavelengths. *Opt. Lett.* **2011**, *36*, 4278–4280.

(7) Kuznetsov, A. I.; Miroshnichenko, A. E.; Brongersma, M. L.; Kivshar, Y. S.; Luk'yanchuk, B. Optically resonant dielectric nanostructures. *Science* **2016**, *354*, aag2472.

(8) Evlyukhin, A. B.; Reinhardt, C.; Seidel, A.; Luk'yanchuk, B. S.; Chichkov, B. N. Optical response features of Si-nanoparticle arrays. *Phys. Rev. B: Condens. Matter Mater. Phys.* **2010**, *82*, 045404.

(9) Garcia-Etxarri, A.; Gomez-Medina, R.; Froufe-Perez, L. S.; Lopez, C.; Chantada, L.; Scheffold, F.; Aizpurua, J.; Nieto-Vesperinas, M.; Sáenz, J. J. Strong magnetic response of submicron silicon particles in the infrared. *Opt. Express* **2011**, *19*, 4815–4826.

(10) Miroshnichenko, A. E.; Luk'yanchuk, B.; Maier, S. A.; Kivshar, Y. S. Optically induced interaction of magnetic moments in hybrid metamaterials. *ACS Nano* **2012**, *6*, 837–842.

(11) Kuznetsov, A. I.; Miroshnichenko, A. E.; Fu, Y. H.; Zhang, J.; Luk'yanchuk, B. Magnetic light. *Sci. Rep.* **2012**, *2*, 492.

(12) Evlyukhin, A. B.; Novikov, S. M.; Zywiets, U.; Eriksen, R. L.; Reinhardt, C.; Bozhevolnyi, S. I.; Chichkov, B. N. Demonstration of magnetic dipole resonances of dielectric nanospheres in the visible region. *Nano Lett.* **2012**, *12*, 3749–3755.

(13) Krasnok, A. E.; Miroshnichenko, A. E.; Belov, P. A.; Kivshar, Y. S. All-dielectric optical nanoantennas. *Opt. Express* **2012**, *20*, 20599–20604.

(14) Albella, P.; Poyli, M. A.; Schmidt, M. K.; Maier, S. A.; Moreno, F.; Sáenz, J. J.; Aizpurua, J. Low-loss Electric and Magnetic Field-Enhanced Spectroscopy with subwavelength silicon dimers. *J. Phys. Chem. C* **2013**, *117*, 13573–13584.

(15) Bakker, R. M.; Permyakov, D.; Yu, Y. F.; Markovich, D.; Paniagua-Domínguez, R.; Gonzaga, L.; Samusev, A.; Kivshar, Y.; Luk'yanchuk, B.; Kuznetsov, A. I. Magnetic and Electric Hotspots with Silicon Nanodimers. *Nano Lett.* **2015**, *15*, 2137–2142.

(16) Slobozhanyuk, A. P.; Poddubny, A. N.; Sinev, I. S.; Samusev, A. K.; Yu, Y. F.; Kuznetsov, A. I.; Miroshnichenko, A. E.; Kivshar, Y. S. Enhanced photonic spin Hall effect with subwavelength topological edge states. *Laser Photon. Rev.* **2016**, *10*, 656–664.

(17) Quidant, R.; Weeber, J. C.; Dereux, A.; Peyrade, D.; Girard, C.; Chen, Y. Spatially resolved photonic transfer through mesoscopic heterowires. *Phys. Rev. E: Stat. Phys., Plasmas, Fluids, Relat. Interdiscip. Top.* **2002**, *65*, 036616.

(18) Burin, A. L.; Cao, H.; Schatz, G. C.; Ratner, M. A. High-quality optical modes in low-dimensional arrays of nanoparticles: application to random lasers. *J. Opt. Soc. Am. B* **2004**, *21*, 121–131.

(19) Blaustein, G. S.; Gozman, M. I.; Samoylova, O.; Polishchuk, I. Y.; Burin, A. L. Guiding optical modes in chains of dielectric particles. *Opt. Express* **2007**, *15*, 17380–17391.

(20) Savelev, R. S.; Slobozhanyuk, A. P.; Miroshnichenko, A. E.; Kivshar, Y. S.; Belov, P. A. Subwavelength waveguides composed of dielectric nanoparticles. *Phys. Rev. B: Condens. Matter Mater. Phys.* **2014**, *89*, 035435.

(21) Savelev, R. S.; Filonov, D. S.; Kapitanova, P. V.; Krasnok, A. E.; Miroshnichenko, A. E.; Belov, P. A.; Kivshar, Y. S. Bending of

electromagnetic waves in all-dielectric particle array waveguides. *Appl. Phys. Lett.* **2014**, *105*, 181116.

(22) Du, J.; Liu, S.; Lin, Z.; Zi, J.; Chui, S. T. Dielectric-based extremely-low-loss subwavelength-light transport at the nanoscale: An alternative to surface-plasmon-mediated waveguiding. *Phys. Rev. A: At, Mol, Opt. Phys.* **2011**, *83*, 035803.

(23) Fan, S.; Joannopoulos, J. D.; Winn, J. N.; Devenyi, A.; Chen, J. C.; Meade, R. D. Guided and defect modes in periodic dielectric waveguides. *J. Opt. Soc. Am. B* **1995**, *12*, 1267–1272.

(24) Halir, R.; Bock, P. J.; Cheben, P.; Ortega-Moñux, A.; Alonso-Ramos, C.; Schmid, J. H.; Lapointe, J.; Xu, D. X.; Wangüemert-Pérez, J. G.; Molina-Fernández, I.; Janz, S. Waveguide sub-wavelength structures: a review of principles and applications. *Laser Photon. Rev.* **2015**, *9*, 25–49.

(25) Bogaerts, W.; Baets, R.; Dumon, P.; Wiaux, V.; Beckx, S.; Taillaert, D.; Luyssaert, B.; Van Campenhout, J.; Bienstman, P.; Van Thourhout, D. Nanophotonic waveguides in silicon-on-insulator fabricated with CMOS technology. *J. Lightwave Technol.* **2005**, *23*, 401–412.

(26) Assefa, S.; Shank, S.; Green, W.; Khater, M.; Kiewra, E.; Reinholm, C.; Kamlapurkar, S.; Rylyakov, A.; Schow, C.; Horst, F.; Pan, H.; et al. A 90nm CMOS integrated nano-photonics technology for 25Gbps WDM optical communications applications. *IEEE International Electron Devices Meeting (IEDM)* **2012**, *33*, 33.8.1.

(27) Orcutt, J. S.; Tang, S. D.; Kramer, S.; Mehta, K.; Li, H.; Stojanović, V.; Ram, R. J. Low-loss polysilicon waveguides fabricated in an emulated high-volume electronics process. *Opt. Express* **2012**, *20*, 7243–7254.

(28) Zhu, S.; Lo, G. Q.; Li, W.; Kwong, D. L. Effect of cladding layer and subsequent heat treatment on hydrogenated amorphous silicon waveguides. *Opt. Express* **2012**, *20*, 23676–23683.

(29) Subramanian, A. Z.; Neutens, P.; Dhakal, A.; Jansen, R.; Claes, T.; Rottenberg, X.; Peyskens, F.; Selvaraja, S.; Helin, P.; Du Bois, B.; Leyssens, K.; et al. Low-loss singlemode PECVD silicon nitride photonic wire waveguides for 532–900 nm wavelength window fabricated within a CMOS pilot line. *IEEE Photonics J.* **2013**, *5*, 2202809–2202809.

(30) Heidel, N. D.; Usechak, N. G.; Dohrman, C. L.; Conway, J. A. A Review of Electronic-Photonic Heterogeneous Integration at DARPA. *IEEE J. Sel. Top. Quantum Electron.* **2016**, *22*, 482–490.

(31) Rybin, M. V.; Filonov, D. S.; Samusev, K. B.; Belov, P. A.; Kivshar, Y. S.; Limonov, M. F. Phase diagram for the transition from photonic crystals to dielectric metamaterials. *Nat. Commun.* **2015**, *6*, 10102.

(32) Joannopoulos, J. D.; Johnson, S. G.; Winn, J. N.; Meade, R. D. *Photonic Crystals: Molding the Flow of Light*, 2nd ed.; Princeton University Press: Princeton, NJ, 2008.

# Resonant Light Guiding Along a Chain of Silicon Nanoparticles

*Reuben M. Bakker<sup>1\*#</sup>, Ye Feng Yu<sup>1#</sup>, Ramón Paniagua-Domínguez<sup>1#</sup>, Boris Luk'yanchuk<sup>1</sup>, Arseniy I. Kuznetsov<sup>1</sup>*

1 Data Storage Institute, A\*STAR (Agency for Science, Technology and Research), 2 Fusionopolis Way, 138634, Singapore

\* [Reuben\\_bakker@dsi.a-star.edu.sg](mailto:Reuben_bakker@dsi.a-star.edu.sg)

# equal contributions

## Supporting Information

Five additional figures are provided as supporting information.

Fig. S1 shows Numerical simulations illustrating the basic modes of the Silicon nanoparticle waveguide with a 50nm gap for the case of real material losses included in the model.

Fig. S2 shows Numerical simulation results illustrating the field distributions of the modes in the dielectric nanoparticle, corresponding to figure 1b.

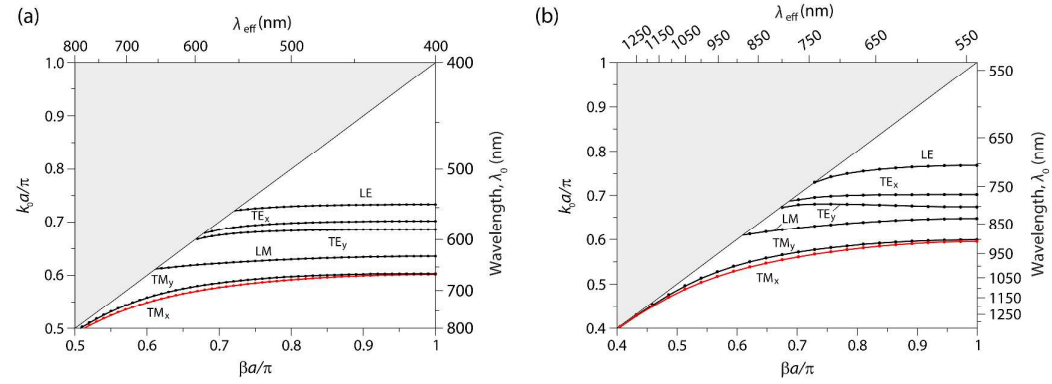
Fig. S3 shows Numerical simulation results illustrating how the Magnetic and Electric modes evolve with wavelength as a function of the nanoparticle height,  $H$ .

Fig. S4 shows : Numerical simulation results illustrating the transmission spectra and power loss through a nanoparticle waveguide.

Fig. S5 shows Numerical simulation results illustrating effective mode area as a function of wavelength for the nanoparticle waveguide.

## Supplementary Figures:

S1:



**Figure S1: Basic Modes of the Silicon Nanoparticle Waveguide with a 50nm gap for 150nm (a) and 220nm (b) dimensioned nanoparticles from numerical calculations including material losses for Silicon. These dispersion plots are complimentary to figure 1 (b,d) in the article, which are calculated for the lossless case.**

S2:

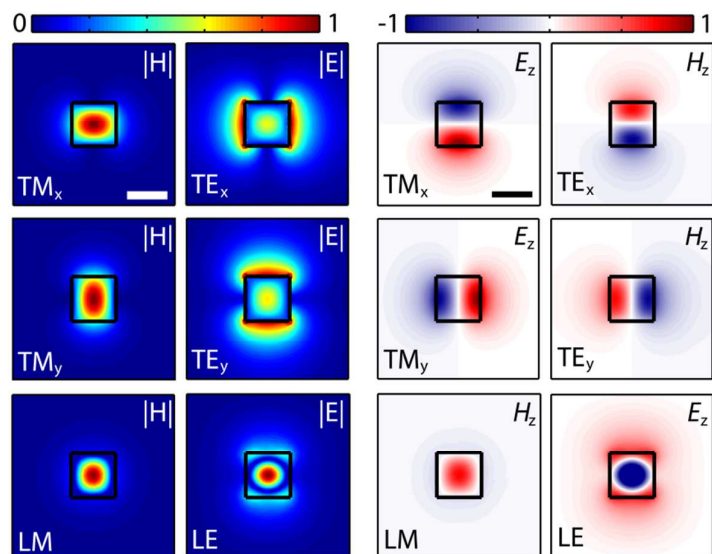


**Figure S2:** Numerical simulation results illustrating the field distributions of the modes in the dielectric nanoparticle, corresponding to figure 1b. Scale bars represent 200 nm.

S3:

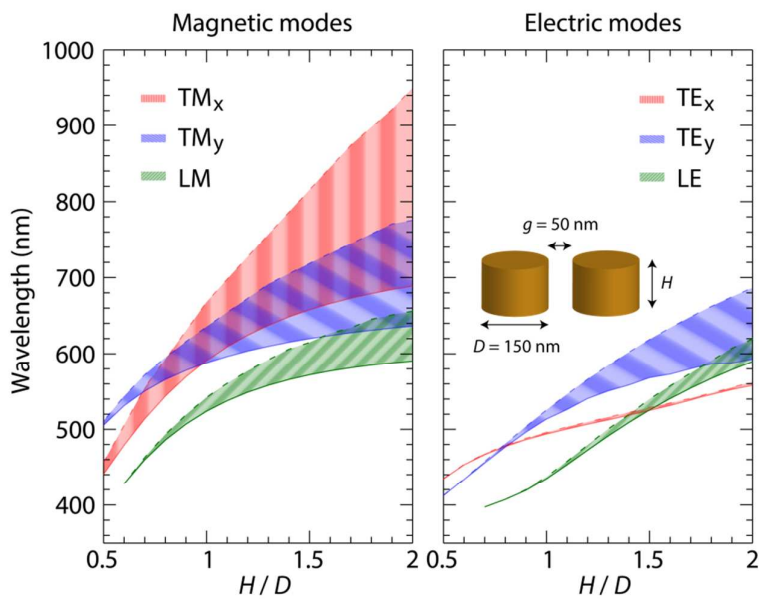


**Figure S3:** Numerical simulation results illustrating how the Magnetic and Electric modes evolve with wavelength as a function of the nanoparticle height,  $H$ . The particles have a fixed diameter  $D = 150$  nm and gap  $g = 50$  nm.

S4:

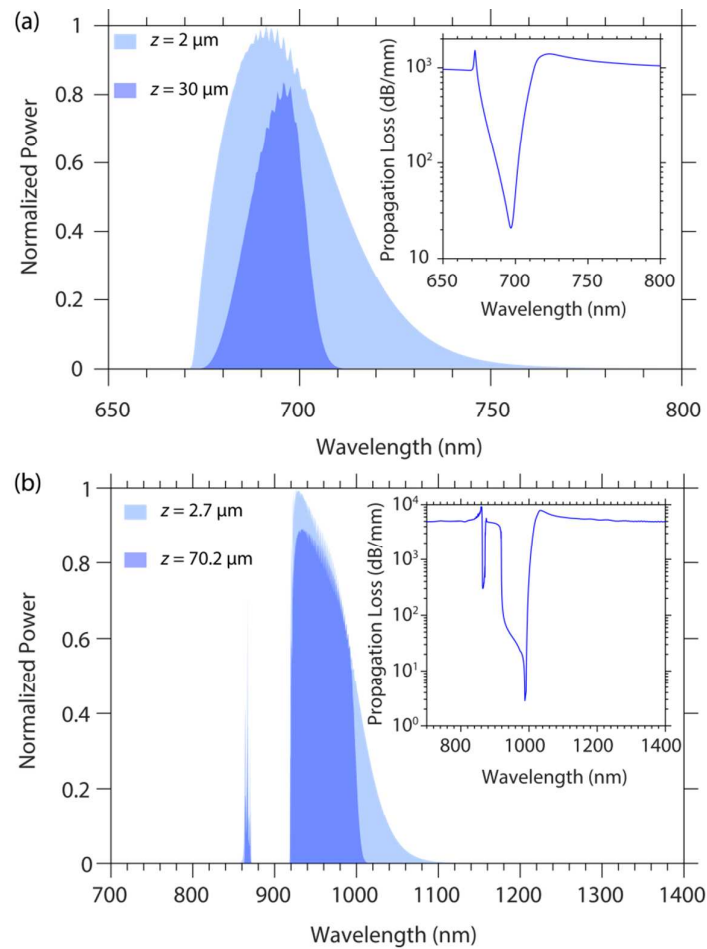


**Figure S4: Numerical simulation results illustrating the transmission spectra and power loss through a nanoparticle waveguide.** **a**, The visible wavelength waveguide consists of 200 nanoparticles (height and diameter equals 150nm, period is 200nm). The plot shows the power on the first monitor, i.e.  $2\mu\text{m}$  away from the origin of the chain, excited by a magnetic dipole source, and a monitor  $30\mu\text{m}$  away from it. The inset shows the loss figure as a function of wavelength. **b**, The NIR wavelength waveguide consists of 300 nanoparticles (height and diameter equals 220nm, period 270nm). The plot shows the power on the first monitor, i.e.  $2.7\mu\text{m}$  away from the origin, and a monitor  $70.2\mu\text{m}$  away from it. The inset shows the loss figure as a function of wavelength. Note the change in shape of the transmitted power for the different chains, similar to those observed in the experiment.

## Supporting Information

S5:

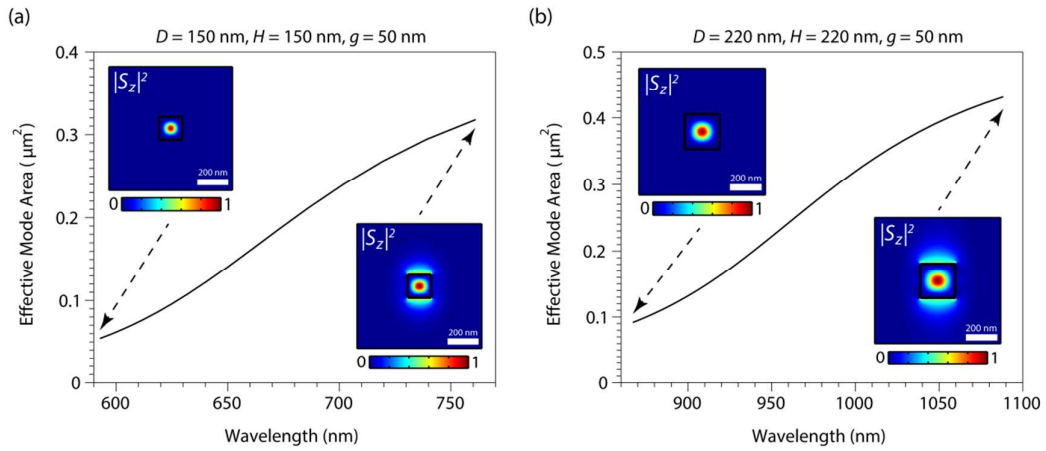


**Figure S5: Numerical simulation results illustrating effective mode area as a function of wavelength for the nanoparticle waveguide. a, The 150nm case for visible light and b, The 220nm case for NIR light. The insets show cross-sectional maps of the absolute value (squared) of the z-component of the Poynting vector (i.e., in the propagation direction) at the lowest and highest wavelengths. Scale bars represent 200 nm.**